

# Broadband omnidirectional light detection in flexible and hierarchical ZnO/Si heterojunction photodiodes

Seongdong Lim<sup>1</sup>, Doo-Seung Um<sup>1</sup>, Minjeong Ha<sup>1</sup>, Qianpeng Zhang<sup>2</sup>, Youngsu Lee<sup>1</sup>, Yuanjing Lin<sup>2</sup>, Zhiyong Fan<sup>2</sup>, and Hyunhyub Ko<sup>1</sup> (✉)

<sup>1</sup> School of Energy and Chemical Engineering, Ulsan National Institute of Science and Technology (UNIST), Ulsan Metropolitan City 44919, Republic of Korea

<sup>2</sup> Department of Electronic and Computer Engineering, Hong Kong University of Science and Technology, Clear Water Bay, Kowloon, Hong Kong, China

Received: 21 June 2016

Revised: 11 August 2016

Accepted: 26 August 2016

© Tsinghua University Press and Springer-Verlag Berlin Heidelberg 2016

## KEYWORDS

flexible photodetector, photodiode, omnidirectional, hierarchical, zinc oxide nanowire

## ABSTRACT

The development of flexible photodetectors has received great attention for future optoelectronic applications including flexible image sensors, biomedical imaging, and smart, wearable systems. Previously, omnidirectional photodetectors were only achievable by integration of a hemispherical microlens assembly on multiple photodetectors. Herein, a hierarchical photodiode design of ZnO nanowires (NWs) on honeycomb-structured Si (H-Si) membranes is demonstrated to exhibit excellent omnidirectional light-absorption ability and thus maintain high photocurrents over broad spectral ranges (365 to 1,100 nm) for wide incident angles (0° to 70°), which enabled broadband omnidirectional light detection in flexible photodetectors. Furthermore, the stress-relieving honeycomb pattern within the photodiode micromembranes provided photodetectors with excellent mechanical flexibility (10% decrease in photocurrent at a bending radius of 3 mm) and durability (minimal change in photocurrent over 10,000 bending cycles). When employed in semiconductor thin films, the hierarchical NW/honeycomb heterostructure design acts as an efficient platform for various optoelectronic devices requiring mechanical flexibility and broadband omnidirectional light detection.

## 1 Introduction

Flexible photodetectors are important for future bendable/foldable electronics for diverse applications such as flexible image sensors [1–3], artificial retina

[4–6], biomedical imaging [7, 8], and smart wearable systems [9–11]. Significant progress has been made in the development of flexible photodetectors based on organic and nanostructured materials such as conducting polymers [3, 12–14], quantum dots [15, 16],

Address correspondence to [hyunhko@unist.ac.kr](mailto:hyunhko@unist.ac.kr)

nanowires (NWs) [17–19], two-dimensional (2D) materials [14, 20–23], and inorganic nanomembranes [24, 25]. These devices exhibit high bendability while providing great photoresponsivity and fast sensing performance. Broadband flexible photodetectors have also been demonstrated [23, 26–31], the properties of which are advantageous in applications such as charge-coupled devices (CCDs), optical communications, remote sensing, astronomy, and defense. However, when flexible photodetectors are employed in curved geometry, most of the incident light is at an oblique angle to the photodetector surfaces, which results in increased light reflectance, thus greatly diminishing the performance of the photodetectors [32–34]. One critical limitation of previous flexible photodetectors has been the lack of omnidirectional light-detection capability, which would provide a wide field-of-view and thus enable precise monitoring of a moving object using light.

The natural light-sensitive organs found in arthropods have evolved into unique imaging systems for sensitive and wide field-of-view light detection. For example, the compound eyes of moths consist of hexagonally-packed, multiple ommatidia on the hemisphere, which enables individual imaging with a large field-of-view [35]. Mimicking the great vision systems in nature, the fabrication of biomimetic image sensors based on microlens arrays omnidirectionally arranged on a hemispherical dome has undergone great progress, resulting in a similar wide field-of-view [4, 5, 36, 37]. However, these photodetectors require special and complicated integration strategies for fabrication of nonplanar sensor arrays. Apart from the use of biomimetic microlens arrays for photodetectors, various structural designs have been suggested for effective omnidirectional light harvesting and achieving enhanced photovoltaic efficiency: for example, antireflective multilayer coatings with graded refractive index [38, 39], antireflective nanostructure designs such as nanodomes [40], inverted nanocones [41], nanopencils [42], and hierarchical micro/nanostructures [43, 44]. Although these structures have been explored for their omnidirectional light-absorption properties in photovoltaic applications, there has been no attempt to demonstrate flexible photodetectors with omnidirectional light-detection capabilities.

Here, we report the first demonstration of a flexible photodetector with both omnidirectional and broadband light-absorption capabilities (the figure-of-merit characteristics of recently reported photodetectors are summarized and compared in Table 1). The device structure is based on the bio-inspired design of hierarchical zinc oxide (ZnO) nanowire (NW) arrays on honeycomb-structured Si (H-Si) membranes, which leads to ZnO NW/H-Si n-p heterojunction structures. In this device design, the hierarchical ZnO NWs on honeycomb structures provide enhanced light-absorption efficiency as well as mechanical flexibility due to the mechanically stable honeycomb structure, which cannot be achieved with traditional crystalline Si membranes. Furthermore, this structure provides omnidirectional light-absorption properties without the use of a hemispherical microlens assembly with multiple photodetectors. The omnidirectional property of flexible photodetectors based on ZnO NWs/H-Si membranes provides stable light detection to furnish a large incident angle range, which enables clear imaging and wide-range detection of objects even though the photodetectors are located on the curved surface. In addition, the ZnO NWs/H-Si photodetectors on flexible polyimide (PI) substrates show stable photodetector performance at a bending radius of 3 mm and over 10,000 bending cycles.

## 2 Experimental

### 2.1 Fabrication of honeycomb-structured Si membranes

Honeycomb patterns with various sizes were formed on a silicon-on-insulator (SOI) wafer via conventional photolithography (MA-6, SUSS MicroTec, Germany) with an AZ nLOF 2035 photoresist. The top Si layer was etched by deep reactive-ion etching (DRIE, Tegal 200, TEGAL, France) with a SiO<sub>2</sub> etch-stop layer for 50 s. The H-Si membrane was spontaneously separated from the mother substrate by selective wet etching with a buffered oxide etch (BOE) solution, which comprised a 6:1 mixture of 40% ammonium fluoride (NH<sub>4</sub>F) and hydrofluoric acid (HF). The separated freestanding Si membrane was rinsed with distilled (DI) water repeatedly.

**Table 1** Comparison of results achieved in this work and previously reported omnidirectional, flexible, and broadband optoelectronics

Type of device	Active layer materials	Omnidirectional property	Flexibility	Detection range (nm)
Solar cell [45]	Si	60% decreased $P_{\max}^a$ at 60° of AOI <sup>b</sup>	—	300–1,100
Solar cell [46]	PEDOT, Si	90% decreased $P_{\max}$ at 60° of AOI <sup>b</sup>	—	400–1,100
Solar cell [44]	Si	60% decreased $P_{\max}$ at 60° of AOI	—	300–1,100
Solar cell [47]	ZnO nanorod, Si	5.3% decreased $J_{sc}^c$ at 60° of AOI	—	400–1,000
PN junction photodiode [22]	Graphene	—	80% $R_p^d$ at $D_B^e = 80^\circ$	>780
PN junction photodiode [48]	ZnO nanorod, PEDOT:PSS	—	Up to $D_B = 75^\circ$	Ultraviolet
Phototransistor [23]	Few-layer InSe	—	50% $R_p$ at $r_B^f = 3$ cm	450–785
Phototransistor [49]	GaS nanosheet	—	Up to $D_B = 60^\circ$	250–600
MSM <sup>g</sup> photodetector [27]	CH <sub>3</sub> NH <sub>3</sub> PbI <sub>3</sub>	—	No data	310–780
MSM photodetector [28]	P3HT:CdSe nanowire	—	No data	350–850
MSM photodetector [29]	PbSe, TiO <sub>2</sub> , graphene	—	Up to $r_B = 6$ mm	300–2,000
Schottky diode [50]	Si, graphene	—	—	200–1,100
Phototransistor [51]	Graphene, Bi <sub>2</sub> Te <sub>3</sub>	—	—	400–1,550
Phototransistor [52]	Few-layer black phosphorus	—	—	Visible to 940
Phototransistor [53]	Graphene	—	—	Visible to mid-IR
MSM photodetector [54]	Graphene quantum dots	—	—	Ultraviolet to near-IR
MSM photodetector [55]	PbS, C <sub>60</sub> fullerite	—	—	400–1,350
MSM photodetector [56]	Few-layer MoS <sub>2</sub>	—	—	380–800
MSM photodetector [57]	ZnO nanowire, Si	—	—	350–800
PN junction photodiode (this work)	ZnO nanowire, Si	30% decreased $I_{PC}^h$ at 70° of AOI	90% $I_{PC}$ at $r_B = 1$ cm	365–1,100

<sup>a</sup> $P_{\max}$ : maximum power; <sup>b</sup>AOI: angle of incidence; <sup>c</sup> $J_{sc}$ : short-circuit current density; <sup>d</sup> $R_p$ : photoresponsivity; <sup>e</sup> $D_B$ : degree of bending curvature; <sup>f</sup> $r_B$ : bending radius; <sup>g</sup>MSM: metal-semiconductor-metal; <sup>h</sup> $I_{PC}$ : photocurrent.

## 2.2 Hydrothermal synthesis of ZnO NWs

A 200-nm-thick uniform ZnO layer was deposited by radio frequency (RF) sputtering under conditions of 500 W and 10 mTorr with O<sub>2</sub> gas at a flow rate of 20 sccm (SRN-120D, SORONA, Korea), as a seed layer to grow ZnO NWs on the fabricated H-Si substrate. The thickness of the deposited ZnO layer was accurately measured by using an ellipsometer (Elli-SE-UaM8, Elipso Technology, Korea). For hydrothermal growth of the ZnO NWs, the growth solution was prepared by mixing equimolar amounts ( $25 \times 10^{-3}$  M) of Zn(NO<sub>3</sub>)<sub>2</sub>·xH<sub>2</sub>O (99.9%, Sigma-Aldrich) and hexamethylenetetramine (HMTA) ( $\geq 99.0\%$ , Sigma-Aldrich)

in DI water with dispersion by sonication. After preheating the growth solution for 5–10 min at 90 °C in a convection oven, the ZnO-deposited H-Si substrates were floated on the surface of the growth solution. The length and diameter of the ZnO NWs were varied by controlling the growth time (Fig. S1 in the Electronic Supplementary Material (ESM)). After the growth step, the surface of the ZnO NWs was rinsed with DI water.

## 2.3 Fabrication of heterojunction photodetector array

Reactive-ion etching (Lab Star, TTL, Korea) followed by photolithography was used to fabricate the arrays

of the H-Si membrane (20 sccm of SF<sub>6</sub>, 60 sccm of Ar, 10 mTorr, 300 W of RF power). After depositing the ZnO layer and growing the ZnO NWs for 1 h on the selectively patterned H-Si membrane, the ZnO NW/Si hetero-structures were annealed at 600 °C by rapid thermal annealing (MILA-5000, ULVAC, USA) to improve the quality of the junction properties. Al (100 nm) and Cr/Au (3 nm/97 nm) were selectively deposited on the ZnO and Si regions to form an ohmic contact by e-beam evaporation (FC-2000, Temescal, USA).

## 2.4 Fabrication of flexible photodetector array

A polyimide (PI) solution was spin coated onto a commercial PI film attached to a glass substrate. Liquid PI was cured at 200 °C on a hot plate for 3 h. A liquid-bridge-mediated transfer printing process was utilized to attach freestanding H-Si membranes to the PI substrate. The prepared freestanding H-Si membranes were fixed on the PI substrate with few drops of ethanol by placing them on a hot plate at 70 °C; thus, the H-Si membranes became tightly attached to the PI surface upon evaporation of the ethanol. Here, the attractive capillary force between the H-Si membrane and PI substrate generated by the evaporation of ethanol induced conformal contact and tight binding between the two substrates. The same process was used to fabricate flexible photodetector arrays with the H-Si/PI substrate, except for the high-temperature rapid thermal annealing (RTA). After depositing the contact metal by e-beam evaporation, RTA was performed at 150 °C to form better junctions between the metal and semiconductor.

## 2.5 Characterizations

The morphologies of the ZnO NWs, H-Si, and hierarchical ZnO NW/H-Si hetero-structures were characterized by field emission scanning electron microscopy (FE-SEM) (S-4800, Hitachi, Japan). The crystal structures of the ZnO layer and ZnO NWs were characterized using a normal X-ray diffractometer (XRD) (D8 Advance, Bruker, USA). The omnidirectional reflection properties of flat Si, H-Si, and ZnO NW/H-Si were verified by UV-Vis-NIR spectroscopy with a variable angle specular reflectance accessory (Cary 5000,

Agilent, USA). Formation of the interface between the ZnO layer and Si was confirmed by high-resolution transmission electron microscopy (HR-TEM) (JEM-2100F, Jeol, Japan). The TEM samples were prepared using a dual-beam focused ion beam (FIB) (Helios NanoLab 450, FEI, USA). The optical images of the H-Si membrane and fabricated photodetectors were characterized by optical microscopy (BX-53, Olympus, Japan).

## 2.6 Electrical and optical measurements

The general electrical characteristics of the hetero-junction photodiodes were measured by using the two-probe method at room temperature (4200-SCS, Keithley, USA). A monochromator (Cornerstone™ 130 1/8 m Monochromators, Newport, USA) with a variable slit and a Xe arc lamp (300 W) was employed to measure the photo-induced current generated upon illumination with various wavelengths of light. To define the relationship between the photocurrent and the optical power of the incident light, the optical power of a commercial 365 nm light-emitting diode (LED) was varied by changing the input voltage into the LED by using a function generator (AFG3011C, Tektronix, USA). The optical intensity of the light source as a function of the wavelength was measured with a calibrated optical power meter (1916-R, Newport, USA) incorporating a Si photodetector (818-UV, Newport, USA) and a Ge photodetector (818-IR, Newport, USA). The fast photoresponse time for the photocurrent was characterized with a source-meter (2450-SCPI, Keithley, USA). The mechanical flexibility and durability were verified by evaluating the bending motion of the flexible photodetector by using a bending tester (JIBT-200, JUNIL TECH, Republic of Korea).

## 2.7 Optical simulation

The finite-difference time-domain (FDTD) method was utilized to simulate the optical properties of the different structures, including flat Si (F-Si), H-Si, ZnO NW/F-Si, and ZnO NW/H-Si. All ZnO NWs had a diameter of 80 nm, a pitch of 200 nm, and a length of 1 μm. In the case of H-Si, the diameter was 8.7 μm. The light source was located at  $z = 2.5 \mu\text{m}$  and was propagated downwards. Normal incidence (0°) and

oblique incidence ( $30^\circ$ ) situations were simulated with periodic boundary conditions (PBCs) and Bloch boundary conditions (BBCs), respectively. Furthermore, the  $|E|^2$  values obtained under 365 and 620 nm excitation were plotted to indicate the light intensity.

### 3 Results and discussion

#### 3.1 Fabrication of omnidirectional ZnO NWs/H-Si n-p junction photodiode

Hierarchical H-Si membrane structures decorated with ZnO NWs were fabricated for use in omnidirectional photodetectors. Figure 1(a) illustrates the fabrication process for the ZnO NWs/H-Si photodetectors on  $\text{SiO}_2/\text{Si}$  substrates. H-Si membranes were fabricated by patterning and etching of commercially available SOI substrates with a 2- $\mu\text{m}$ -thick p-Si top layer (resistivity range: 1–5 Ohm-cm). For growth of the hierarchical ZnO NW arrays on H-Si membranes, a ZnO seed film (200 nm thick) was deposited by using a RF magnetron sputtering system with  $\text{O}_2$ , and ZnO NWs were subsequently grown by using a hydrothermal method [58–60]. The SEM images of the sputtered ZnO layer and the hydrothermally grown ZnO NWs with different growth times are presented in Figs. S1(a) and S1(b) (in the ESM), which show the densely packed and regular grain sizes of the ZnO crystals in the seed layer and the vertically aligned ZnO NWs grown on the seed layer. The length and diameter of the ZnO NWs could be precisely controlled by controlling the growth time (Figs. S1(c) and S1(d) in the ESM). The ZnO NWs were uniformly grown on H-Si membranes, resulting in hierarchical ZnO NWs/H-Si structures (Fig. 1(b)). XRD analysis of both the ZnO seed layer and the ZnO NWs in Fig. S1(e) (in the ESM) shows the highest (002) plane peak and three minor peaks of the (100), (101), and (102) planes, resulting from the *c*-axis crystal growth and the hexagonal symmetry of the wurtzite structure. The cross-sectional HR-TEM images in Fig. S2(a) (in the ESM) confirm epitaxial growth of the ZnO NWs on the ZnO seed films with a well-matched (002) growth plane with a lattice spacing of 0.26 nm. After growing the ZnO NWs on H-Si, Al (~100 nm thickness) and Cr/Au (3 nm/97 nm) electrodes were deposited on the ZnO NWs and H-Si

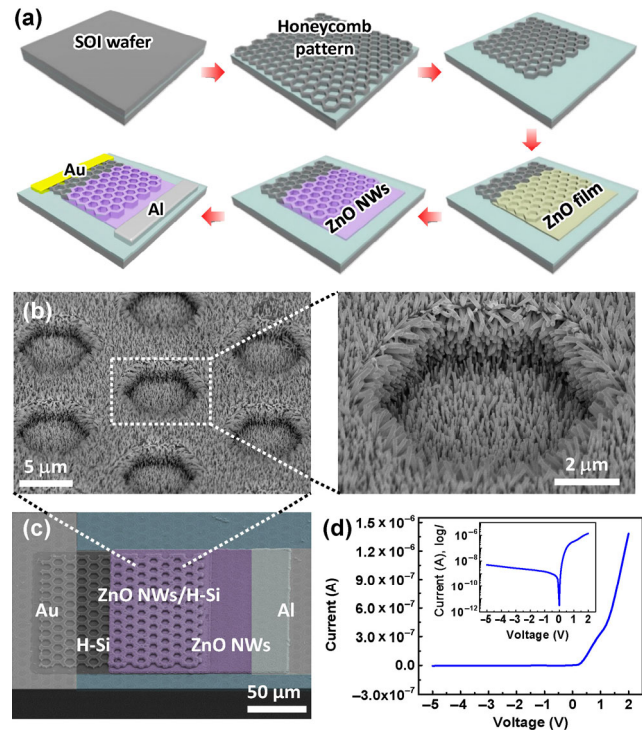


**Figure 1** Hierarchical design of H-Si decorated with ZnO NWs. (a) Schematic illustration of the fabrication of ZnO NW/H-Si on  $\text{SiO}_2/\text{Si}$  substrate. (b) Tilted SEM image of ZnO NWs on H-Si structure (diameter: 8.7  $\mu\text{m}$ ). (c) Tilted SEM image of ZnO NW/H-Si photodiode. (d)  $I$ - $V$  curve for ZnO NW/H-Si photodiode in dark state (without illumination). Inset shows a log current-linear voltage plot ( $\log I$ - $V$ ).

area, respectively, to form an ohmic contact (Fig. S3 in the ESM shows the linear  $I$ - $V$  curves of Al-ZnO-Al and Cr/Au-Si-Cr/Au). Here, Al deposition increased the number of oxygen defects of the ZnO layer due to the formation of  $\text{Al}_2\text{O}_3$  at the interface between Al and ZnO [61], which improved the forward current of the diode device due to the surface doping effects.

Figure 1(c) shows the tilted-view SEM image of the ZnO NW/H-Si photodiode on the  $\text{SiO}_2/\text{Si}$  substrate. The Si-ZnO interface in the n-p ZnO NW/H-Si hetero-structure was investigated by cross-sectional HR-TEM image analysis. The results show a sharp Si-ZnO interface and a thin native  $\text{SiO}_2$  layer (Fig. S2(b) in the ESM) [62]. Formation of the high-quality ZnO/Si junction in the n-p ZnO NW/H-Si hetero-structure was also confirmed by analyzing the current versus voltage ( $I$ - $V$ ) plot in Fig. 1(d), which shows a high rectification ratio of ~160 at an applied voltage of 2 V. The current in the forward biased region

(0.2–2 V) increased exponentially in accord with the relation  $I \approx \exp(\alpha V)$ . This behavior indicates charge transport by a recombination tunneling mechanism that is commonly observed for wide-band-gap p–n diodes [63]. The ideality factor of 3.1 was calculated from the slope of the low forward bias condition (red line in Fig. S4 in the ESM) using the following equation

$$n = \frac{q}{kT} \left( \frac{\partial V}{\partial \ln I} \right) \quad (1)$$

where  $k$  is Boltzmann's constant,  $T$  is the temperature in Kelvin, and  $q$  is the electron charge. The large value for the ideality factor results from the heterojunction comprising different band gap materials and the formation of an interfacial oxide layer. The obtained value is still adequate in comparison with the ideality factors of previously studied ZnO/Si heterojunctions (2.4, 3.18, and 3.91) [64–66].

### 3.2 Optoelectronic characteristics of ZnO NW/H-Si n–p junction photodiode

Figure 2 shows the typical photoresponsive properties of the n–p ZnO NW/H-Si photodetectors on SiO<sub>2</sub>/Si substrates (the transfer curves of the field-effect

transistors based on n-type ZnO NWs and p-type H-Si channel materials are presented in Fig. S5 (in the ESM)). The  $I$ – $V$  curves in Fig. 2(a) indicate that the photocurrent generated under reverse bias increased significantly and was dependent on the illuminating light. Figure S7 in the ESM shows the energy band diagram of the n-ZnO/p-Si heterojunction [67, 68]. Visible and NIR light mainly pass through the ZnO layer and are absorbed in the depleted p-Si region, which generates photo-induced electrons. On the other hand, UV light is absorbed in the ZnO region and generates photo-induced holes. Under reverse bias conditions, the generated photo-induced minority carriers can flow and are collected at the electrode in response to an external electric field, resulting in an increase of the current (generation of photocurrent). The photocurrent generated under 570 nm illumination is much larger than that generated under 365 and 620 nm illumination with same light intensity of 800  $\mu\text{W}\cdot\text{cm}^{-2}$ . This result coincides with the spectral photoresponsivity data presented in Fig. 2(b). The photodiodes exhibit a broad spectral range from the UV to NIR region, and the spectral photoresponsivity has a maximum at 540 nm. The wavelength of highest photoresponsivity was blue-shifted in comparison to

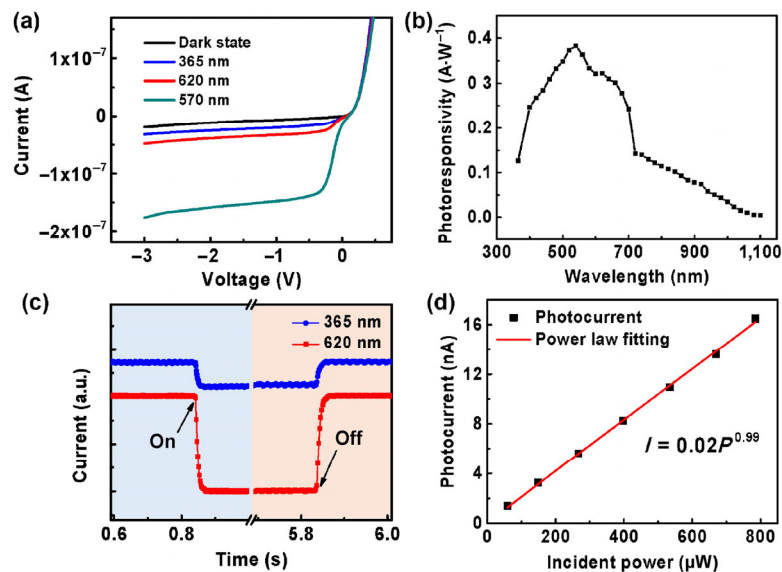


**Figure 2** Photoresponsive properties of ZnO NW/H-Si photodiodes. (a)  $I$ – $V$  curves for reverse-biased region under dark conditions and with illumination at three different wavelengths (the optical power of the incident light was 800  $\mu\text{W}\cdot\text{cm}^{-2}$ ). (b) Spectral photoresponsivity of ZnO NW/H-Si photodiode spanning UV to NIR wavelength range at an applied voltage of -2 V. (c) Photoresponse time of ZnO NW/H-Si photodiode under illumination at 365 and 620 nm. (d) Dependence of photoresponse on different illumination intensities under illumination at 365 nm at an applied voltage of -2 V.

that of the H-Si based photodetectors (the spectral photoresponsivity data for the metal-semiconductor-metal photodetector based on the H-Si membrane are presented in Fig. S6 (in the ESM)), which can be attributed to the enhanced UV photoresponsivity conferred by the ZnO NWs [69]. The relatively low photoresponsivity at wavelengths over 700 nm is a consequence of the reduced thickness of the Si membrane because the penetration depth of the incident light is dependent on the wavelength, and wavelengths over 700 nm cannot be sufficiently absorbed by the thin Si membrane (2  $\mu\text{m}$  thickness). Si membranes show reduced absorption of red and NIR light when the thickness decreases [70]. Optimization of the thickness of the Si membrane enables achievement of a better photoresponse in the NIR region in comparison with this result.

Figure 2(c) and Fig. S8 (in the ESM) indicate the fast response time ( $\sim 11$  ms rise time and  $\sim 12$  ms decay time) of the ZnO NW/H-Si photodiodes under illumination with both UV and visible light due to the p-n junction photodetection mechanism. It was also confirmed that the response time is similar for both ZnO NW/H-Si and ZnO NW/F-Si regardless of the structural difference between the Si photodiodes (Figs. S8(a)–S8(d) in the ESM). This result can be favorably compared to that obtained with conventional ZnO photodetectors, which show a slow response time ( $>100$  s) and a narrow UV response range mainly because of the surface oxygen adsorption/desorption mechanism in the photodetection processes [71, 72]. The repeatability of the photoresponse under illumination with 365 and 620 nm light indicates the stability of the photodiodes (Fig. S8(e) in the ESM). To investigate the generation and recombination behavior of the photo-induced current under incident light, the photocurrent was measured as a function of the optical power of the incident light (Fig. 2(d)). The exponent  $\theta$  in the power law relation ( $I_{\text{ph}} \approx P^\theta$ ) provides information on the generation and recombination behavior of a photo-induced current [73]. A  $\theta$  value of unity indicates the ideal state, where the photo-induced current increases linearly with increasing incident power. The value of  $\theta$  falls below unity depending on the number of trap states in the photodetector [74]. The developed photodiode exhibits a near-ideal power

relation with  $\theta = 0.99$  (Fig. 2(d)), which indicates excellent junction properties with a low density of trap states between ZnO and Si. In accordance with the near-ideal power relation, the  $I$ - $V$  curve of ZnO NW/H-Si (Fig. S9 in the ESM) showed no hysteresis behavior, which indicates a small amount of charge trap states at the junction.

The photoresponsivity of the ZnO NW/Si heterostructured photodiodes depends on the chamber environment during sputtering of the ZnO layer and depends on the growth time of the ZnO NWs. In particular, the number of oxygen vacancies in the sputtered ZnO layer affects the photoresponsivity. A ZnO layer sputtered under an  $\text{O}_2$  environment has better crystallinity with a smaller number of oxygen vacancies than a ZnO layer without an  $\text{O}_2$  environment. As shown in Fig. S10(a) (in the ESM), the ZnO NW/Si photodetectors based on the ZnO layer sputtered under an  $\text{O}_2$  environment showed a higher photoresponsive on/off ratio than those based on the ZnO layer sputtered under a  $\text{N}_2$  environment. This result can be attributed to the reduced dark current (reverse saturation current) in p-n junction diodes, resulting from the improved quality of the ZnO film [75]. The generation and recombination of carriers decreases with prolonged minority carrier lifetime because the high-crystallinity ZnO layer forms a good interface with Si, thus the reverse current decreases [76–78]. The growth time of the ZnO NWs also affects the photoresponsivity of the ZnO NW/Si photodetectors. Figure S10(b) in the ESM shows the increase of both the dark current and ON current as a function of the growth time. The increase of the growth time results in a decrease of the photoresponsive on/off ratio (Fig. S10(a) in the ESM), which can be attributed to the increase of the dark current with the increasing crystallinity of the ZnO NWs. The high crystallinity of the ZnO NWs results in less carrier scattering during the transport process, thus reducing the possibility of recombination of drift carriers through the NWs to the electrode [79]. The increase of the crystallinity of the ZnO NWs with increasing growth time can be confirmed from the XRD data presented in Fig. S10(c) (in the ESM), where the intensity of the (002) peaks increases with increasing growth time. Notably, the enhanced intensity of the (002) peaks is mainly

attributed to the increased crystallinity of the ZnO NWs with increasing growth time, not to the amount of ZnO NWs. It was also observed that the increased growth time induced a slight increase of the photocurrent (Fig. S10(d) in the ESM). The slight increase of the photocurrent can be attributed to effective light scattering and absorption by the ZnO NW arrays, which enhances light absorption in the ZnO/Si junction area. However, the predominant increase of the dark current compared to the ON current results in a decrease of the photoresponse on/off ratio with increasing growth time (Fig. S10(e) in the ESM).

### 3.3 Characterization of omnidirectional property of ZnO NWs/H-Si photodetector

To evaluate the omnidirectional light-detection capability of the hierarchical ZnO NW/H-Si hetero-junction photodiodes (Fig. 3(a)), four different types of hetero-structured photodiodes (ZnO film/F-Si, ZnO film/H-Si, ZnO NWs/F-Si, and ZnO NWs/H-Si) were fabricated. All four types of photodiodes showed clear rectification behavior and high photocurrent in the reverse-biased region (Fig. S11 in the ESM). The variation of the photocurrent (PC) (the photocurrent ratio at an incident angle to normal incidence,  $I_A/I_0$ ) depending on the angle of incident light at 620 nm shown in Fig. 3(b), indicates the excellent omnidirectional light-detection ability of the hierarchical ZnO NW/H-Si structure as compared to those of the other structures ( $I_0$  of ZnO film/F-Si, ZnO film/H-Si, ZnO NWs/F-Si, and ZnO NWs/H-Si was 120, 102, 115, and 96.8 nA, respectively). The photocurrent of the ZnO film/F-Si photodiode decreased sharply ( $I_A/I_0 = 0.1$  over  $60^\circ$ ) with increasing incident angle of light. In the case of the ZnO NW/F-Si diode, the photocurrent decreased below  $I_A/I_0 = 0.4$  at an incident angle of  $70^\circ$ , despite the omnidirectional light absorption ability of the NW structures due to the graded refractive index profile from air to the bottom layer of the ZnO NWs [57, 80]. For the ZnO film/H-Si structures, the device showed better omnidirectional light-detection ability than the ZnO Film/F-Si structures, which can be attributed to the role of H-Si to effectively absorb and guide the direction of the incident light even at high incident angles via scattering processes [81, 82]. Thus, the photocurrent of the hierarchical ZnO NW/H-Si

structures was maintained above  $I_A/I_0 = 0.7$  at an incident angle of  $70^\circ$  as compared to the photocurrent at normal incident angle ( $I_0$ ). These results indicate that the hierarchical structures of the NWs on the honeycomb Si micropatterns can enhance the light absorption, as well as the omnidirectional property. The higher omnidirectionality of the hierarchical ZnO NW/H-Si structures as compared to the ZnO NW/F-Si structures can be attributed to the effective light absorption and guidance of the honeycomb structures. In addition, antireflective ZnO NW arrays with hierarchical structures enable excellent light absorption. Therefore, hierarchical ZnO NW/H-Si photodetectors show the best omnidirectional light-detection ability in comparison to the other structures.

To investigate the effects of the size of the hexagonal holes on the omnidirectional light-detection ability of

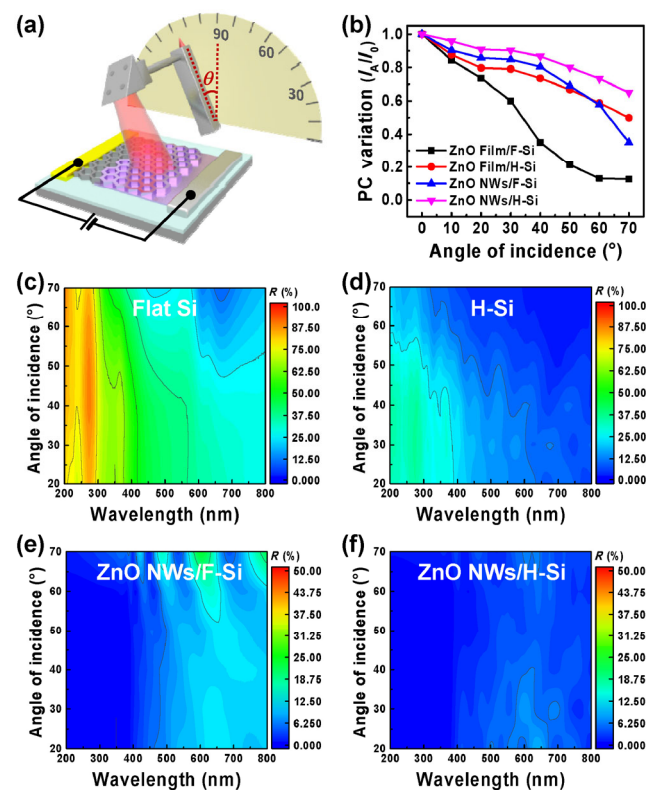


**Figure 3** Omnidirectional light-absorption properties of hierarchical hetero-structures of ZnO NWs on H-Si. (a) Photocurrent measurement system as a function of angle of incident light. (b) Variation of photocurrent for four different hetero-structured ZnO/Si photodiodes as a function of angle of incident light at 620 nm. 2D plots of UV–Vis–NIR reflectance data for (c) F-Si, (d) H-Si, (e) ZnO NWs on F-Si, and (f) ZnO NWs on 8.7  $\mu\text{m}$  H-Si using variable angle specular reflectance accessory.

the honeycomb structures, hierarchical structures with four different hole sizes were prepared (Fig. S12 in the ESM). The omnidirectional light-detection ability was enhanced with increasing size of the hexagonal holes (Fig. S13 in the ESM). At low incident angles (below  $40^\circ$ ), the variation of the photocurrent as a function of the incident angle was similar for all hole sizes. However, at high incident angles (over  $40^\circ$ ), the larger hexagonal holes showed better omnidirectionality because greater light absorption and scattering was possible with the larger holes. As seen in Fig. S14 (in the ESM), at a low angle of incidence ( $30^\circ$ ), light absorption occurred throughout the honeycomb structure, regardless of the size of the hexagonal holes. However, at an intermediate angle of incidence ( $45^\circ$ ), light absorption did not occur at the bottom parts of the honeycomb structures for the smaller hexagonal holes ( $2.2 \mu\text{m}$ ). Furthermore, at a high incident angle ( $60^\circ$ ), light absorption occurred only at the wall of the honeycomb structure for the smaller hexagonal holes ( $2.2 \mu\text{m}$ ). For the larger hexagonal holes ( $8.7 \mu\text{m}$ ), light absorption occurred at both the wall and the bottom of the honeycomb structure, even at a high incident angle ( $60^\circ$ ), resulting in minimal photocurrent variation as compared to that at low incident angles. Therefore, hexagonal hole arrays with larger holes provide better omnidirectionality than structures with smaller hexagonal holes.

To further investigate the omnidirectional light-absorption ability of the hierarchical ZnO NW/H-Si structures, the angle-dependent light-absorption properties of four different structures were compared, i.e., F-Si, H-Si, ZnO NW/F-Si, and ZnO NW/H-Si, by using UV-Vis-NIR spectroscopy with a variable angle specular reflectance accessory (VASRA) (Figs. 3(c)–3(f)). Here, the spectroscopic data show the reflectance of light with incident angles from  $20^\circ$  to  $70^\circ$ . For the F-Si substrates, although the reflectance of UV light was above  $\sim 50\%$ , the reflectance in the visible/NIR range was lower than that of the UV region due to the absorption of visible/NIR light by Si (Fig. 3(c)). H-Si showed much lower reflectance in the UV to visible/NIR region than F-Si (Fig. 3(d)), which is attributed to the increased light scattering and absorption of the hexagonal hole arrays. For the ZnO NWs grown on F-Si, the reflectance of UV light declined remarkably

below 5% due to absorption of UV light by the ZnO NWs, as well as the large decrease in the reflectance in the visible/NIR region due to light scattering by the nanowire structures (Fig. 3(e)). For the ZnO NWs grown on H-Si, the hierarchical ZnO NW/H-Si structures exhibited excellent omnidirectional light-absorption ability with greatly diminished reflectance over the entire spectral range from UV to NIR (Fig. 3(f)), which can be attributed to the combined effects of the ZnO NWs and the honeycomb Si structure. The reflectance data obtained with VASRA are in good agreement with the angle-dependent photocurrent variation.

To further elucidate the morphology-dependent omnidirectional light absorption behavior, the  $|E|^2$  distribution for various morphologies was calculated by the FDTD method. Figure 4 shows the cross-sectional  $|E|^2$  distribution at 620 nm with an angle of incidence of  $30^\circ$  for different morphologies. As compared to F-Si, the H-Si structure provided scattering-induced multiple light absorption, resulting in enhancement of the E-fields on the surface of Si

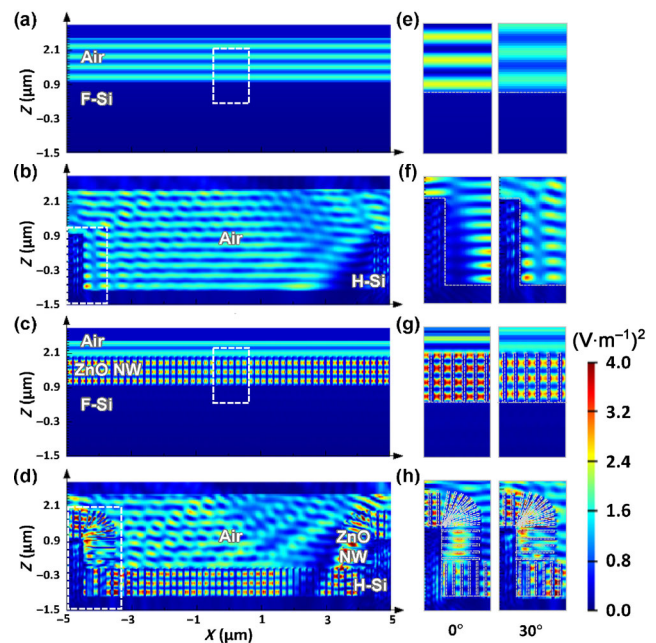


**Figure 4** Simulated cross-sectional  $|E|^2$  distribution of the electromagnetic (EM) wave at 620 nm excitation with different morphologies: (a) F-Si, (b) H-Si, (c) ZnO NW/F-Si, and (d) ZnO NW/H-Si at angular incidence of  $30^\circ$ . Magnified view of EM wave distribution with different morphologies: (e) F-Si, (f) H-Si, (g) ZnO NW/F-Si, and (h) ZnO NW/H-Si (left: normal incidence, right:  $30^\circ$  incidence).

(Figs. 4(a) and 4(b)). As shown in Fig. 4(c), strong E-field resonances occurred between the ZnO NWs on F-Si, which improved the light absorption. In accordance with the results, the additional ZnO NWs on H-Si dramatically enhanced the E-fields on the surface of ZnO NW/H-Si (Fig. 4(d)). Figures 4(e)–4(h) show a comparison of the E-field intensity distributions at 620 nm excitation with normal incidence and 30° incidence. For the ZnO NW/F-Si structure, the resonance of the E-field between the ZnO NWs was stronger with normal incidence than with 30° incidence. However, the E-field inside the honeycomb structures with normal incidence was smaller than that with 30° incidence due to the weaker light scattering effect. This result indicates that the light scattering effect in the honeycomb structures is beneficial for E-field enhancement.

### 3.4 Mechanical flexibility and durability of ZnO NW/H-Si photodetector on PI substrate

Figure 5(a) shows photographic and optical microscopy (OM) images of a free-standing H-Si membrane rolled on the tip of a pipette, which confirms the excellent flexibility of the H-Si membrane. To fabricate flexible photodetectors, we utilized liquid-bridge-mediated transfer printing to attach the separated H-Si membrane

onto the flexible PI substrate [83]. In the liquid-bridge-mediated printing process, the attractive capillary force generated between the H-Si membrane and the PI substrate by solvent evaporation induces conformal contact and tight binding between the two substrates. Figure 5(b) shows a photograph and schematic illustration of the flexible ZnO NW/H-Si photodetector arrays on the PI substrate. The flexible photodetector showed high rectification behavior ( $\sim 74$  at an applied voltage of 3 V) and photocurrent in the reverse-biased region under illumination with 365 nm light (Fig. S15 in the ESM). Notably, the honeycomb structures enabled uniform distribution of the external mechanical strain to the triangular region, thus providing excellent mechanical stability [84]. The flexibility of the developed hierarchical-structured, flexible photodiode on the PI substrate was proven by mechanical bending tests as a function of the bending curvature, as shown in Fig. S16 (in the ESM). The ZnO NW/H-Si flexible photodiodes showed stable photoresponsive properties without a significant change of the  $I$ - $V$  curve at a high bending curvature ( $r_B = 0.415$  cm) (Fig. 5(c)). With increasing bending curvature, the photocurrent was maintained at up to 90% of the initial photocurrent at a bending radius of 3 mm (Fig. 5(d)). This behavior is attributed to the advantageous honeycomb structure

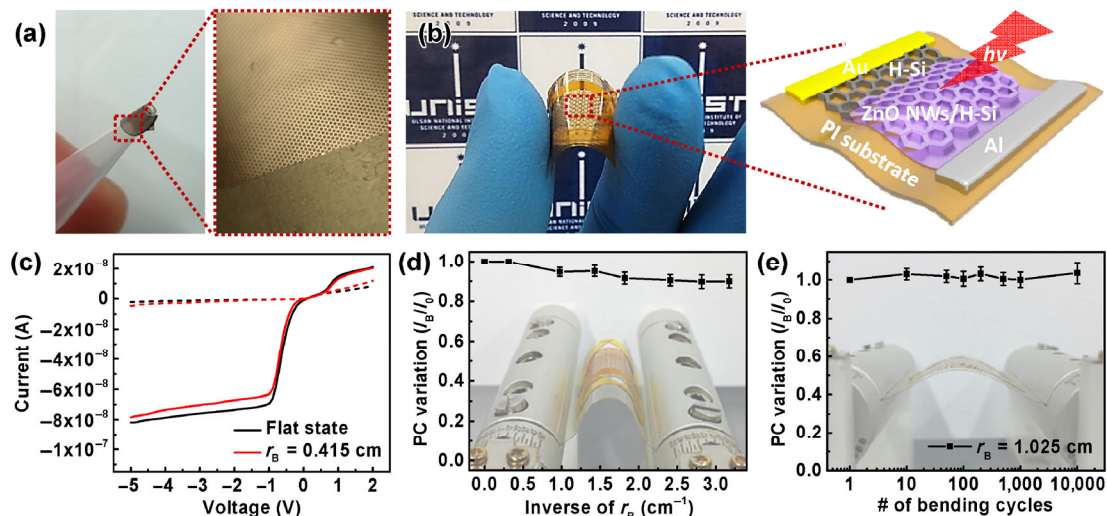


**Figure 5** Evaluation of flexibility and durability of flexible ZnO NW/H-Si photodiode on PI substrate. (a) Digital images and OM image of rolled H-Si membrane on tip of pipette. (b) Photograph and schematic showing the highly flexible ZnO NW/H-Si-based photodiode on polyimide. (c)  $I$ - $V$  curves of flexible photodiode in dark state (dotted line) and under illumination with 365 nm light (solid line) as a function of the bending curvature. (d) Variation of photocurrent with increasing bending curvature. (Background photograph shows photodiode bent with bending machine ( $r_B = 0.415$  cm).) (e) Mechanical durability of ZnO NW/H-Si photodiode on PI substrate with increasing number of bending cycles with a bending radius of  $r_B = 1.025$  cm.

that provides better mechanical flexibility [84, 85]. The ZnO NW/H-Si flexible photodiodes also showed extremely high mechanical durability. As seen in Fig. 5(e), the photodetector provided stable dark/ON currents and minimal photocurrent variations for 10,000 bending cycles. SEM analysis of the photodetector after 10,000 bending cycles did not show any mechanical failures such as cracks or delamination of the ZnO NWs from the ZnO NW/H-Si photodetectors (Fig. S17 in the ESM).

## 4 Conclusion

In summary, a highly efficient flexible photodetector with omnidirectional and broadband light-detection capability was developed by using an ultraflexible and hierarchical ZnO nanowire/Si honeycomb photodiode membrane. The developed ZnO NW/H-Si-based photodiodes have a fast response time of ~11 ms and a broad photoresponse range spanning the UV to NIR. Notably, the developed hierarchical ZnO NWs on the H-Si membrane can detect omnidirectional light (maintain high photocurrents up to incident angles of 70°), which was previously achievable only with complicated nonplanar photodetectors with microlens arrays in previous reports. Furthermore, the device fabricated with the honeycomb-structured Si membrane resulted in flexible photodetectors with high mechanical flexibility and durability with minimal photocurrent variation. We anticipate that the developed omnidirectional and flexible photodetectors based on hierarchically structured honeycomb micromembranes will find numerous applications for high-performance flexible optoelectronic systems such as wearable electronics, artificial retina, bio-medical imaging, and future energy harvesting.

## Acknowledgements

This work was supported by the National Research Foundation of Korea (Nos. 2011-0014965 and 2015R1A2A1A10054152), the Center for Advanced Soft-Electronics funded by the Ministry of Science, ICT and Future Planning as Global Frontier Project (No. 2015M3A6A5065314), the Ministry of Trade,

Industry and Energy (No. 10064058), General Research Fund (No. 612113) from Hong Kong Research Grant Council, Innovation and Technology Fund (No. ITS/362/14FP) from the Innovation and Technology Commission of Hong Kong, and State Key Laboratory on Advanced Displays and Optoelectronics at HKUST.

**Electronic Supplementary Material:** Supplementary material (SEM images, statistics, XRD analysis of ZnO NWs as a function of growth time, HR-TEM analysis of the interface between ZnO NWs and ZnO film and between ZnO film and Si,  $I$ - $V$  curves of Al-ZnO-Al and Cr/Au-Si-Cr/Au, a natural log  $I$ - $V$  ( $\ln I$ - $V$ ) curve for ZnO NW/H-Si photodiode in dark state, transfer curves of field-effect transistors based on ZnO NW and H-Si, spectral photoresponsivity of metal-semiconductor-metal photodetector based on H-Si, energy band diagrams of p-Si/n-ZnO heterojunction photodiode, repeated photoresponse results,  $I$ - $V$  hysteresis curve of ZnO NWs/H-Si photodiode, photoresponsivity as a function of the growth condition of ZnO NWs (sputtering gas environment for ZnO film, growth time),  $I$ - $V$  curves for three different kinds of hetero-structured ZnO/Si photodiodes, cross-sectional SEM images of H-Si, and ZnO NW/H-Si according to the size of the hexagonal hole, comparison of omnidirectional light-detection capability as a function of the size of the hexagonal hole, schematics for light paths with incident angles of 30°, 45°, and 60° into different sizes of hexagonal hole,  $I$ - $V$  curves of ZnO NW/H-Si photodiode on PI substrate, digital images of bent photodiode arrays on PI substrate as a function of the bending radius, SEM images of ZnO NWs/H-Si photodiode on PI substrate after 10,000 cycles of mechanical bending test at bending radius of 1 cm) is available in the online version of this article at <http://dx.doi.org/10.1007/s12274-016-1263-y>.

## References

- [1] Nau, S.; Wolf, C.; Sax, S.; List-Kratochvil, E. J. W. Organic non-volatile resistive photo-switches for flexible image detector arrays. *Adv. Mater.* **2015**, *27*, 1048–1052.
- [2] Zhang, L.; Wu, T.; Guo, Y.; Zhao, Y.; Sun, X.; Wen, Y.; Yu, G.; Liu, Y. Large-area, flexible imaging arrays constructed by light-charge organic memories. *Sci. Rep.* **2013**, *3*, 1080.

- [3] Someya, T.; Kato, Y.; Iba, S.; Noguchi, Y.; Sekitani, T.; Kawaguchi, H.; Sakurai, T. Integration of organic FETs with organic photodiodes for a large area, flexible, and lightweight sheet image scanners. *IEEE Trans. Electron Devices* **2005**, *52*, 2502–2511.
- [4] Floreano, D.; Pericet-Camara, R.; Viollet, S.; Ruffier, F.; Bruckner, A.; Leitel, R.; Buss, W.; Menouni, M.; Expert, F.; Juston, R. et al. Miniature curved artificial compound eyes. *Proc. Natl. Acad. Sci. USA* **2013**, *110*, 9267–9272.
- [5] Ko, H. C.; Stoykovich, M. P.; Song, J. Z.; Malyarchuk, V.; Choi, W. M.; Yu, C. J.; Geddes, J. B.; Xiao, J. L.; Wang, S. D.; Huang, Y. G. et al. A hemispherical electronic eye camera based on compressible silicon optoelectronics. *Nature* **2008**, *454*, 748–753.
- [6] Lee, L. P.; Szema, R. Inspirations from biological optics for advanced photonic systems. *Science* **2005**, *310*, 1148–1150.
- [7] Lochner, C. M.; Khan, Y.; Pierre, A.; Arias, A. C. All-organic optoelectronic sensor for pulse oximetry. *Nat. Commun.* **2014**, *5*, 5745.
- [8] Lee, C. M.; Engelbrecht, C. J.; Soper, T. D.; Helmchen, F.; Seibel, E. J. Scanning fiber endoscopy with highly flexible, 1 mm catheterscopes for wide-field, full-color imaging. *J. Biophotonics* **2010**, *3*, 385–407.
- [9] Huang, S. Y.; Guo, C. F.; Zhang, X.; Pan, W.; Luo, X.; Zhao, C. S.; Gong, J. H.; Li, X. Y.; Ren, Z. F.; Wu, H. Buckled tin oxide nanobelt webs as highly stretchable and transparent photosensors. *Small* **2015**, *11*, 5712–5718.
- [10] Gao, Y.; Sim, K.; Sun, S. C.; Chen, Z.; Song, J. Z.; Yu, C. J. Crack-insensitive wearable electronics enabled through high-strength kevlar fabrics. *IEEE Trans. Compon., Packag., Manuf. Technol.* **2015**, *5*, 1230–1236.
- [11] Wang, Z. R.; Wang, H.; Liu, B.; Qiu, W. Z.; Zhang, J.; Ran, S. H.; Huang, H. T.; Xu, J.; Han, H. W.; Chen, D. et al. Transferable and flexible nanorod-assembled TiO<sub>2</sub> cloths for dye-sensitized solar cells, photodetectors, and photocatalysts. *ACS Nano* **2011**, *5*, 8412–8419.
- [12] Rim, Y. S.; Yang, Y. M.; Bae, S. H.; Chen, H. J.; Li, C.; Goorsky, M. S.; Yang, Y. Ultrahigh and broad spectral photodetectivity of an organic–inorganic hybrid phototransistor for flexible electronics. *Adv. Mater.* **2015**, *27*, 6885–6891.
- [13] Pace, G.; Grimoldi, A.; Natali, D.; Sampietro, M.; Coughlin, J. E.; Bazan, G. C.; Caironi, M. All-organic and fully-printed semitransparent photodetectors based on narrow bandgap conjugated molecules. *Adv. Mater.* **2014**, *26*, 6773–6777.
- [14] Jang, S.; Hwang, E.; Lee, Y.; Lee, S.; Cho, J. H. Multifunctional graphene optoelectronic devices capable of detecting and storing photonic signals. *Nano Lett.* **2015**, *15*, 2542–2547.
- [15] Sun, Z. H.; Liu, Z. K.; Li, J. H.; Tai, G. A.; Lau, S. P.; Yan, F. Infrared photodetectors based on CVD-grown graphene and PbS quantum dots with ultrahigh responsivity. *Adv. Mater.* **2012**, *24*, 5878–5883.
- [16] Lee, J. S.; Kovalenko, M. V.; Huang, J.; Chung, D. S.; Talapin, D. V. Band-like transport, high electron mobility and high photoconductivity in all-inorganic nanocrystal arrays. *Nat. Nanotechnol.* **2011**, *6*, 348–352.
- [17] Xie, X. M.; Shen, G. Z. Single-crystalline In<sub>2</sub>S<sub>3</sub> nanowire-based flexible visible-light photodetectors with an ultra-high photoresponse. *Nanoscale* **2015**, *7*, 5046–5052.
- [18] Tian, W.; Zhang, C.; Zhai, T. Y.; Li, S. L.; Wang, X.; Liu, J. W.; Jie, X.; Liu, D. Q.; Liao, M. Y.; Koide, Y. et al. Flexible ultraviolet photodetectors with broad photoresponse based on branched ZnS-ZnO heterostructure nanofilms. *Adv. Mater.* **2014**, *26*, 3088–3093.
- [19] Liu, X.; Gu, L. L.; Zhang, Q. P.; Wu, J. Y.; Long, Y. Z.; Fan, Z. Y. All-printable band-edge modulated ZnO nanowire photodetectors with ultra-high detectivity. *Nat. Commun.* **2014**, *5*, 4007.
- [20] Zheng, W. S.; Xie, T.; Zhou, Y.; Chen, Y. L.; Jiang, W.; Zhao, S. L.; Wu, J. X.; Jing, Y. M.; Wu, Y.; Chen, G. C. et al. Patterning two-dimensional chalcogenide crystals of Bi<sub>2</sub>Se<sub>3</sub> and In<sub>2</sub>Se<sub>3</sub> and efficient photodetectors. *Nat. Commun.* **2015**, *6*, 6972.
- [21] Yuan, X.; Tang, L.; Liu, S. S.; Wang, P.; Chen, Z. G.; Zhang, C.; Liu, Y. W.; Wang, W. Y.; Zou, Y. C.; Liu, C. et al. Arrayed van der Waals vertical heterostructures based on 2D GaSe grown by molecular beam epitaxy. *Nano Lett.* **2015**, *15*, 3571–3577.
- [22] Liu, N.; Tian, H.; Schwartz, G.; Tok, J. B. H.; Ren, T. L.; Bao, Z. Large-area, transparent, and flexible infrared photodetector fabricated using p–n junctions formed by N-doping chemical vapor deposition grown graphene. *Nano Lett.* **2014**, *14*, 3702–3708.
- [23] Tamalampudi, S. R.; Lu, Y. Y.; Kumar, U. R.; Sankar, R.; Liao, C. D.; Moorthy, B. K.; Cheng, C. H.; Chou, F. C.; Chen, Y. T. High performance and bendable few-layered InSe photodetectors with broad spectral response. *Nano Lett.* **2014**, *14*, 2800–2806.
- [24] Seo, J.-H.; Oh, T.-Y.; Park, J.; Zhou, W. D.; Ju, B.-K.; Ma, Z. Q. A multifunction heterojunction formed between pentacene and a single-crystal silicon nanomembrane. *Adv. Funct. Mater.* **2013**, *23*, 3398–3403.
- [25] Yuan, H.-C.; Shin, J.; Qin, G. X.; Sun, L.; Bhattacharya, P.; Lagally, M. G.; Celler, G. K.; Ma, Z. Q. Flexible photodetectors on plastic substrates by use of printing transferred single-crystal germanium membranes. *Appl. Phys. Lett.* **2009**, *94*, 013102.

- [26] Liu, Y. L.; Yu, C. C.; Lin, K. T.; Yang, T. C.; Wang, E. Y.; Chen, H. L.; Chen, L. C.; Chen, K. H. Transparent, broadband, flexible, and bifacial-operable photodetectors containing a large-area graphene-gold oxide heterojunction. *ACS Nano* **2015**, *9*, 5093–5103.
- [27] Hu, X.; Zhang, X. D.; Liang, L.; Bao, J.; Li, S.; Yang, W. L.; Xie, Y. High-performance flexible broadband photodetector based on organolead halide perovskite. *Adv. Funct. Mater.* **2014**, *24*, 7373–7380.
- [28] Wang, X. F.; Song, W. F.; Liu, B.; Chen, G.; Chen, D.; Zhou, C. W.; Shen, G. Z. High-performance organic–inorganic hybrid photodetectors based on P3HT:CdSe nanowire heterojunctions on rigid and flexible substrates. *Adv. Funct. Mater.* **2013**, *23*, 1202–1209.
- [29] Manga, K. K.; Wang, J. Z.; Lin, M.; Zhang, J.; Nesladek, M.; Nalla, V.; Ji, W.; Loh, K. P. High-performance broadband photodetector using solution-processible PbSe-TiO<sub>2</sub>-graphene hybrids. *Adv. Mater.* **2012**, *24*, 1697–1702.
- [30] Hu, K.; Chen, H. Y.; Jiang, M. M.; Teng, F.; Zheng, L. X.; Fang, X. S. Broadband photoresponse enhancement of a high-performance t-Se microtube photodetector by plasmonic metallic nanoparticles. *Adv. Funct. Mater.*, in press, DOI: 10.1002/adfm.201602408.
- [31] Chen, H. Y.; Liu, H.; Zhang, Z. M.; Hu, K.; Fang, X. S. Nanostructured photodetectors: From ultraviolet to terahertz. *Adv. Mater.* **2016**, *28*, 403–433.
- [32] Wang, A.; Gill, P.; Molnar, A. Light field image sensors based on the talbot effect. *Appl. Opt.* **2009**, *48*, 5897–5905.
- [33] Martin, N.; Ruiz, J. M. Calculation of the PV modules angular losses under field conditions by means of an analytical model. *Sol. Energy Mater. Sol. Cells* **2001**, *70*, 25–38.
- [34] Courtial, J.; Oxburgh, S.; Tyc, T. Direct stigmatic imaging with curved surfaces. *J. Opt. Soc. Am. A* **2015**, *32*, 478–481.
- [35] Ko, D.-H.; Tumbleston, J. R.; Henderson, K. J.; Euliss, L. E.; DeSimone, J. M.; Lopez, R.; Samulski, E. T. Biomimetic microlens array with antireflective “moth-eye” surface. *Soft Matter* **2011**, *7*, 6404–6407.
- [36] Jeong, K. H.; Kim, J.; Lee, L. P. Biologically inspired artificial compound eyes. *Science* **2006**, *312*, 557–561.
- [37] Song, Y. M.; Xie, Y. Z.; Malyarchuk, V.; Xiao, J. L.; Jung, I.; Choi, K. J.; Liu, Z. J.; Park, H.; Lu, C. F.; Kim, R. H. et al. Digital cameras with designs inspired by the arthropod eye. *Nature* **2013**, *497*, 95–99.
- [38] Fang, C.-Y.; Liu, Y.-L.; Lee, Y.-C.; Chen, H.-L.; Wan, D.-H.; Yu, C.-C. Nanoparticle stacks with graded refractive indices enhance the omnidirectional light harvesting of solar cells and the light extraction of light-emitting diodes. *Adv. Funct. Mater.* **2013**, *23*, 1412–1421.
- [39] Yan, X.; Poxson, D. J.; Cho, J.; Welsler, R. E.; Sood, A. K.; Kim, J. K.; Schubert, E. F. Enhanced omnidirectional photovoltaic performance of solar cells using multiple-discrete-layer tailored- and low-refractive index anti-reflection coatings. *Adv. Funct. Mater.* **2013**, *23*, 583–590.
- [40] Ou, Y. Y.; Zhu, X. L.; Jokubavicius, V.; Yakimova, R.; Mortensen, N. A.; Syväjärvi, M.; Xiao, S. S.; Ou, H. Y. Broadband antireflection and light extraction enhancement in fluorescent SiC with nanodome structures. *Sci. Rep.* **2014**, *4*, 4662.
- [41] Lin, Q. F.; Leung, S. F.; Lu, L. F.; Chen, X. Y.; Chen, Z.; Tang, H. N.; Su, W. J.; Li, D. D.; Fan, Z. Y. Inverted nanocone-based thin film photovoltaics with omnidirectionally enhanced performance. *ACS Nano* **2014**, *8*, 6484–6490.
- [42] Lin, H.; Xiu, F.; Fang, M.; Yip, S.; Cheung, H. Y.; Wang, F. Y.; Han, N.; Chan, K. S.; Wong, C. Y.; Ho, J. C. Rational design of inverted nanopencil arrays for cost-effective, broadband, and omnidirectional light harvesting. *ACS Nano* **2014**, *8*, 3752–3760.
- [43] Wu, W. Q.; Feng, H. L.; Rao, H. S.; Xu, Y. F.; Kuang, D. B.; Su, C. Y. Maximizing omnidirectional light harvesting in metal oxide hyperbranched array architectures. *Nat. Commun.* **2014**, *5*, 3968.
- [44] Wang, H. P.; Lin, T. Y.; Hsu, C. W.; Tsai, M. L.; Huang, C. H.; Wei, W. R.; Huang, M. Y.; Chien, Y. J.; Yang, P. C.; Liu, C. W. et al. Realizing high-efficiency omnidirectional n-type Si solar cells via the hierarchical architecture concept with radial junctions. *ACS Nano* **2013**, *7*, 9325–9335.
- [45] Wang, H. P.; Lin, T. Y.; Tsai, M. L.; Tu, W. C.; Huang, M. Y.; Liu, C. W.; Chueh, Y. L.; He, J. H. Toward efficient and omnidirectional n-type Si solar cells: Concurrent improvement in optical and electrical characteristics by employing microscale hierarchical structures. *ACS Nano* **2014**, *8*, 2959–2969.
- [46] Wei, W. R.; Tsai, M. L.; Ho, S. T.; Tai, S. H.; Ho, C. R.; Tsai, S. H.; Liu, C. W.; Chung, R. J.; He, J. H. Above-11%-efficiency organic–inorganic hybrid solar cells with omnidirectional harvesting characteristics by employing hierarchical photon-trapping structures. *Nano Lett.* **2013**, *13*, 3658–3663.
- [47] Lin, C. A.; Lai, K. Y.; Lien, W. C.; He, J. H. An efficient broadband and omnidirectional light-harvesting scheme employing a hierarchical structure based on a ZnO nanorod/Si<sub>3</sub>N<sub>4</sub>-coated Si microgroove on 5-inch single crystalline Si solar cells. *Nanoscale* **2012**, *4*, 6520–6526.
- [48] Manekthodi, A.; Lu, M. Y.; Wang, C. W.; Chen, L. J. Direct growth of aligned zinc oxide nanorods on paper substrates for low-cost flexible electronics. *Adv. Mater.* **2010**, *22*, 4059–4063.

- [49] Hu, P. A.; Wang, L. F.; Yoon, M.; Zhang, J.; Feng, W.; Wang, X. N.; Wen, Z. Z.; Idrobo, J. C.; Miyamoto, Y.; Geohegan, D. B. et al. Highly responsive ultrathin GaS nanosheet photodetectors on rigid and flexible substrates. *Nano Lett* **2013**, *13*, 1649–1654.
- [50] An, X. H.; Liu, F. Z.; Jung, Y. J.; Kar, S. Tunable graphene-silicon heterojunctions for ultrasensitive photodetection. *Nano Lett* **2013**, *13*, 909–916.
- [51] Qiao, H.; Yuan, J.; Xu, Z. Q.; Chen, C. Y.; Lin, S. H.; Wang, Y. S.; Song, J. C.; Liu, Y.; Khan, Q.; Hoh, H. Y. et al. Broadband photodetectors based on graphene-Bi<sub>2</sub>Te<sub>3</sub> heterostructure. *ACS Nano* **2015**, *9*, 1886–1894.
- [52] Buscema, M.; Groenendijk, D. J.; Blanter, S. I.; Steele, G. A.; van der Zant, H. S.; Castellanos-Gomez, A. Fast and broadband photoresponse of few-layer black phosphorus field-effect transistors. *Nano Lett* **2014**, *14*, 3347–3352.
- [53] Zhang, Y. Z.; Liu, T.; Meng, B.; Li, X. H.; Liang, G. Z.; Hu, X. N.; Wang, Q. J. Broadband high photoresponse from pure monolayer graphene photodetector. *Nat. Commun.* **2013**, *4*, 1811.
- [54] Tang, L. B.; Ji, R. B.; Li, X. M.; Bai, G. X.; Liu, C. P.; Hao, J. H.; Lin, J. Y.; Jiang, H. X.; Teng, K. S.; Yang, Z. B. et al. Deep ultraviolet to near-infrared emission and photoresponse in layered N-doped graphene quantum dots. *ACS Nano* **2014**, *8*, 6312–6320.
- [55] Saran, R.; Nordin, M. N.; Curry, R. J. Facile fabrication of PbS nanocrystal: C<sub>60</sub> fullerite broadband photodetectors with high detectivity. *Adv. Funct. Mater.* **2013**, *23*, 4149–4155.
- [56] Tsai, D. S.; Liu, K. K.; Lien, D. H.; Tsai, M. L.; Kang, C. F.; Lin, C. A.; Li, L. J.; He, J. H. Few-layer MoS<sub>2</sub> with high broadband photogain and fast optical switching for use in harsh environments. *ACS Nano* **2013**, *7*, 3905–3911.
- [57] Tsai, D. S.; Lin, C. A.; Lien, W. C.; Chang, H. C.; Wang, Y. L.; He, J. H. Ultra-high-responsivity broadband detection of Si metal-semiconductor-metal schottky photodetectors improved by ZnO nanorod arrays. *ACS Nano* **2011**, *5*, 7748–7753.
- [58] Greene, L. E.; Law, M.; Goldberger, J.; Kim, F.; Johnson, J. C.; Zhang, Y. F.; Saykally, R. J.; Yang, P. D. Low-temperature wafer-scale production of ZnO nanowire arrays. *Angew. Chem. Int. Ed.* **2003**, *42*, 3031–3034.
- [59] Ko, H.; Zhang, Z. X.; Takei, K.; Javey, A. Hierarchical polymer micropillar arrays decorated with ZnO nanowires. *Nanotechnology* **2010**, *21*, 295305.
- [60] Ha, M.; Lim, S.; Park, J.; Um, D.-S.; Lee, Y.; Ko, H. Bioinspired interlocked and hierarchical design of ZnO nanowire arrays for static and dynamic pressure-sensitive electronic skins. *Adv. Funct. Mater.* **2015**, *25*, 2841–2849.
- [61] Kim, H.-K.; Kim, K.-K.; Park, S.-J.; Seong, T.-Y.; Adesida, I. Formation of low resistance nonalloyed Al/Pt ohmic contacts on n-type ZnO epitaxial layer. *J. Appl. Phys.* **2003**, *94*, 4225–4227.
- [62] Huang, C.-Y.; Yang, Y.-J.; Chen, J.-Y.; Wang, C.-H.; Chen, Y.-F.; Hong, L.-S.; Liu, C.-S.; Wu, C.-Y. p-Si nanowires/SiO<sub>2</sub>/n-ZnO heterojunction photodiodes. *Appl. Phys. Lett.* **2010**, *97*, 013503.
- [63] Ghosh, R.; Basak, D. Electrical and ultraviolet photoresponse properties of quasisaligned ZnO nanowires/p-Si heterojunction. *Appl. Phys. Lett.* **2007**, *90*, 243106.
- [64] Hwang, J. D.; Chen, Y. H. Carrier transport mechanism on ZnO nanorods/p-Si heterojunction diodes with various atmospheres annealing hydrothermal seed-layer. *Thin Solid Films* **2012**, *520*, 5409–5412.
- [65] Yakuphanoglu, F.; Caglar, Y.; Caglar, M.; Ilican, S. ZnO/p-Si heterojunction photodiode by sol-gel deposition of nanostructure n-ZnO film on p-Si substrate. *Mat. Sci. Semicon. Proc.* **2010**, *13*, 137–140.
- [66] Klason, P.; Rahman, M. M.; Hu, Q. H.; Nur, O.; Turan, R.; Willander, M. Fabrication and characterization of p-Si/n-ZnO heterostructured junctions. *Microelect. J.* **2009**, *40*, 706–710.
- [67] Mridha, S.; Basak, D. Ultraviolet and visible photoresponse properties of n-ZnO/p-Si heterojunction. *J. Appl. Phys.* **2007**, *101*, 083102.
- [68] Bai, Z. M.; Yan, X. Q.; Chen, X.; Cui, Y.; Lin, P.; Shen, Y. W.; Zhang, Y. Ultraviolet and visible photoresponse properties of a ZnO/Si heterojunction at zero bias. *RSC Adv.* **2013**, *3*, 17682–17688.
- [69] Liao, Q. L.; Liang, M. Y.; Zhang, Z.; Zhang, G. J.; Zhang, Y. Strain-modulation and service behavior of Au-MgO-ZnO ultraviolet photodetector by piezo-phototronic effect. *Nano Res.* **2015**, *8*, 3772–3779.
- [70] Sharma, M.; Pudasaini, P. R.; Ruiz-Zepeda, F.; Elam, D.; Ayon, A. A. Ultrathin, flexible organic-inorganic hybrid solar cells based on silicon nanowires and PEDOT:PSS. *ACS Appl. Mater. Interfaces* **2014**, *6*, 4356–4363.
- [71] Soci, C.; Zhang, A.; Xiang, B.; Dayeh, S. A.; Aplin, D. P. R.; Park, J.; Bao, X. Y.; Lo, Y. H.; Wang, D. ZnO nanowire UV photodetectors with high internal gain. *Nano Lett.* **2007**, *7*, 1003–1009.
- [72] Dhara, S.; Giri, P. K. ZnO nanowire heterostructures: Intriguing photophysics and emerging applications. *Rev. Nanosci. Nanotechnol.* **2013**, *2*, 147–170.
- [73] Kind, H.; Yan, H. Q.; Messer, B.; Law, M.; Yang, P. D. Nanowire ultraviolet photodetectors and optical switches. *Adv. Mater.* **2002**, *14*, 158–160.
- [74] Zeng, L. H.; Wang, M. Z.; Hu, H.; Nie, B.; Yu, Y. Q.; Wu, C. Y.; Wang, L.; Hu, J. G.; Xie, C.; Liang, F. X. et al. Monolayer graphene/germanium schottky junction as high-performance self-driven infrared light photodetector. *ACS*

- Appl. Mater. Interfaces* **2013**, *5*, 9362–9366.
- [75] Qi, H. X.; Li, Q. S.; Zhao, B.; Zheng, M. M.; Li, X. S.; Zhang, N. Influence of ZnO homobuffer layer on n-ZnO/p-Si photodiode. *Mater. Sci. Technol.* **2008**, *24*, 1002–1004.
- [76] Schubert, E. F. *Light-Emitting Diodes*, 2nd ed.; Cambridge University Press: Cambridge, UK, 2006.
- [77] Liu, Y.; Gorla, C. R.; Liang, S.; Emanetoglu, N.; Lu, Y.; Shen, H.; Wraback, M. Ultraviolet detectors based on epitaxial ZnO films grown by MOCVD. *J. Electron. Mater.* **2000**, *29*, 69–74.
- [78] Sieg, R. M.; Carlin, J. A.; Boeckl, J. J.; Ringel, S. A.; Currie, M. T.; Ting, S. M.; Langdo, T. A.; Taraschi, G.; Fitzgerald, E. A.; Keyes, B. M. High minority-carrier lifetimes in GaAs grown on low-defect-density Ge/GeSi/Si substrates. *Appl. Phys. Lett.* **1998**, *73*, 3111–3113.
- [79] Ridhuan, N. S.; Razak, K. A.; Lockman, Z.; Abdul Aziz, A. Structural and morphology of ZnO nanorods synthesized using ZnO seeded growth hydrothermal method and its properties as UV sensing. *PLoS One* **2012**, *7*, e50405.
- [80] Chao, Y. C.; Chen, C. Y.; Lin, C. A.; Dai, Y. A.; He, J. H. Antireflection effect of ZnO nanorod arrays. *J. Mater. Chem.* **2010**, *20*, 8134–8138.
- [81] Zhao, J. H.; Wang, A. H.; Green, M. A.; Ferrazza, F. 19.8% efficient “honeycomb” textured multicrystalline and 24.4% monocrystalline silicon solar cells. *Appl. Phys. Lett.* **1998**, *73*, 1991–1993.
- [82] Sai, H.; Saito, K.; Kondo, M. Investigation of textured back reflectors with periodic honeycomb patterns in thin-film silicon solar cells for improved photovoltaic performance. *IEEE J. Photovolt.* **2013**, *3*, 5–10.
- [83] Hwang, J. K.; Cho, S.; Dang, J. M.; Kwak, E. B.; Song, K.; Moon, J.; Sung, M. M. Direct nanoprinting by liquid-bridge-mediated nanotransfer moulding. *Nat. Nanotechnol.* **2010**, *5*, 742–748.
- [84] Davami, K.; Zhao, L.; Lu, E.; Cortes, J.; Lin, C.; Lilley, D. E.; Purohit, P. K.; Bargatin, I. Ultralight shape-recovering plate mechanical metamaterials. *Nat. Commun.* **2015**, *6*, 10019.
- [85] Takahashi, T.; Takei, K.; Gillies, A. G.; Fearing, R. S.; Javey, A. Carbon nanotube active-matrix backplanes for conformal electronics and sensors. *Nano Lett.* **2011**, *11*, 5408–5413.